

Multi-band Bose-Einstein condensate at four-particle scattering resonance

Joe Bailey^{*,1,2}, Pavlo Sukhachov^{†,3,4}, Korbinian Baumgaertl^{†,5,6}, Simone Finizio¹, Sebastian Wintz^{1,7}, Carsten Dubs⁸, Joerg Raabe¹, Dirk Grundler^{5,6}, Alexander Balatsky^{9,4} and Gabriel Aeppli^{*,1,2,10}

([†]denotes equal contribution, *corresponding authors)

1. Paul Scherrer Institut, Villigen, PSI CH-5232, Switzerland
2. Institut de Physique, EPFL, Lausanne, CH-1015, Switzerland
3. Department of Physics, Yale University, New Haven, CT 06520, USA
4. Nordita, KTH Royal Institute of Technology and Stockholm University, Roslagstullsbacken 23, SE-106 91 Stockholm, Sweden
5. Laboratory of Nanoscale Magnetic Materials and Magnonics, Institute of Materials (IMX)
6. Institute of Microengineering (IMT), École Polytechnique Fédérale de Lausanne (EPFL), 1015 Lausanne, Switzerland
7. Max-Planck-Institute for Intelligent Systems, D70569 Stuttgart, Germany
8. INNOVENT e.V. Technologieentwicklung Jena, 07745 Jena, Germany
9. Department of Physics and Institute for Materials Science, University of Connecticut, Storrs, CT 06269, USA
10. Department of Physics, ETH Zürich, Zürich, CH-8093, Switzerland

Superfluidity and superconductivity are macroscopic manifestations of quantum mechanics, which have continuously fascinated scientists since their discoveries roughly a century ago. Here the organization of identical particles is represented by a complex-valued condensate wavefunction whose squared amplitude corresponds to the density which by itself would be sufficient to describe a classical fluid. Ever since the initial theories¹⁻⁴ of such quantum fluids were formulated, there has been speculation as to the possibility of multi-component quantum order, where the wavefunction would be a vector or tensor assembled from several complex numbers⁵⁻⁷. A particularly simple multi-component condensate is built from particles occupying different quantum states, or bands, prior to condensation. The particles in one or both bands may undergo condensation, as seen for certain solids and anticipated for particular cold atom systems⁸⁻¹⁰. For bulk solids (containing electrons which condense as pairs), the different bands always order simultaneously, with conventional pairing characterized by complex order parameters describing the

condensates in each band. Another type of condensate, notable for occurring at room temperature, has been identified for spin waves (also called magnons), the magnetic analogue of lattice vibrations, injected by microwaves into high-quality yttrium iron garnet crystals¹¹. Here we show that magnon quantization for thin samples results in a new multi-band magnon condensate. We establish a phase diagram, as a function of microwave drive power and frequency relative to the magnon bands, revealing both single and multi-band condensation. The most stable multi-band condensate is found in a narrow regime favoured on account of a resonance in the scattering between magnons in two bands. Our discovery introduces a flexible non-equilibrium solid state platform operating at room temperature for a well-characterised and easily sourced material, exploiting a Feshbach-like resonance, for examining multi-band phenomena. It points to qualitatively new ways to engineer and control condensates and superconducting states in multiband systems and potential devices containing multiple interacting condensates.

Multiband solid-state systems are a theme of great interest in modern condensed matter, providing routes both to higher temperature and other exotic superconductivity as well as to topological matter. They can manifest strong correlations between fluids which are only weakly coupled in their normal states, and also encode more information in the higher dimensional vector or tensor representing the local values of the macroscopic wavefunction. Realisations are uncommon however, with potential systems identified for cold atoms¹², and experiments performed on certain exotic superconductors starting¹³ with SrTiO₃ and much later including iron chalcogenides⁹, rare-earth intermetallics¹⁴, and MgB₂^{10,15}. Two-dimensional systems emerging near interfaces (or surfaces) are a fertile venue for such condensates because confinement along the direction perpendicular to the interface results in distinct quantum levels which, when motion parallel to the interface is taken into account, form distinct two-dimensional bands. Examples where occupancy of more than one quantum well state affects two-dimensional superconductivity are Al/InAs, much celebrated as hosting possible Majorana edge modes^{16,17}, and LaAlO₃/SrTiO₃ interfaces¹⁸. For the former, the multi-state occupancy is considered a nuisance for topological quantum computing¹⁹, and for the latter, the superconducting order peaks at the Lifschitz transition (boundary) between single- and multi-state occupancy. The results for pair condensates in two-dimensional electronic systems, found so far only at very low, sub-Kelvin temperatures, raise two questions, the first asking whether such phenomena can be seen at room temperature, and the second concerned with the possibility of analogous two-dimensional Bose-Einstein condensates (BEC). In this paper, we answer both questions in the affirmative. Specifically, magnons, also referred to as spin waves, in a thin ferromagnet are bosons which occupy multiple quantum well states, and with microwave pumping, can achieve simultaneous Bose-Einstein condensation at room temperature.

Figure 1 illustrates the basic physics of our experiments. We start by considering magnons in a thin ferromagnetic film for which backward volume (BV) dipole-exchange magnon modes are quantized over the thickness of the film (see figure 1 **a**). Figure 1 **b** shows the bowl-like dispersion surfaces as a function of the in-plane wavevector k for the two lowest modes (referred to by the indices, $n = 0$ and $n = 1$). The key features are minima away from the $k = 0$ zone centre, which exist for both modes although they are substantially shallower for the first excited quantum well state; the coherent occupancy of such minima corresponds to Bose-Einstein condensation of magnons. For low microwave power, single magnons can be injected with accessible momenta largely determined by the antenna geometry. At higher powers, however, magnons will appear in pairs with opposite momentum, relaxing the dependence on antenna geometry, and with a net energy equal to the pump frequency (orange markers in figure 1 **b**). The subsequent formation of condensates then depends on

scattering among the magnons to feed the band minima. What is new for two-band systems is resonant four-magnon (two magnons in, two magnons out) scattering, with the scattering amplitude between two pumped magnons in the lower band to two magnons, one in the upper and one in the lower bands being maximized for pumped magnon pairs at a resonance frequency approximately midway between the minima. Figure 1 **c** shows the corresponding Feynman diagram and the imaginary part of the first-order correction to this four-magnon scattering amplitude $\Psi_{1,2;3,4}$. Here, $\Omega = \omega_1 + \omega_2 = \omega_3 + \omega_4$ and $\mathbf{K} = \mathbf{k}_1 + \mathbf{k}_2 = \mathbf{k}_3 + \mathbf{k}_4$ are the total frequencies and momenta of the scattered magnons respectively. Furthermore, we set $\mathbf{K} = \mathbf{0}$, which corresponds to scattering from a pair of pumped magnons created from a single photon. There is a noticeable peak in the scattering amplitude for a pump frequency close to the sum of two band minima, $\Omega \approx \omega_{\min n=0} + \omega_{\min n=1}$. In fact, the resonant frequency is slightly above this because conservation of momentum does not permit scattering directly into both the $n = 0$ and $n = 1$ minima simultaneously. The peak indicates the resonant enhancement for the multiple scattering amplitude and of course will be further amplified as higher-order terms are taken into account. The explicit expression for the imaginary part of the scattering amplitude is given in the methods with further discussion in the section 4 of the Supplementary Information (SI).

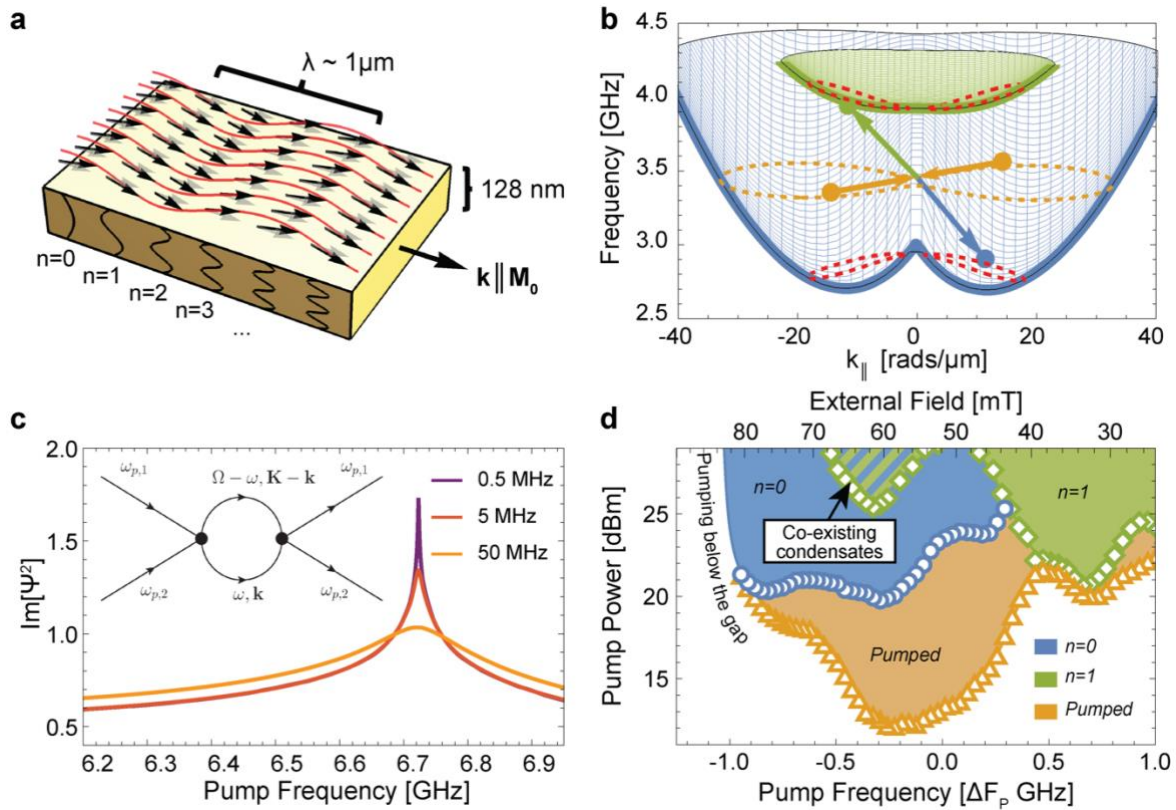


Figure 1: Magnon dispersion and dynamics in thin YIG films. **a** We study backward volume (BV) dipole-exchange magnons ($k \parallel M_0$) in 128nm thick YIG films. In such films, the quantization of magnon modes over the film thickness plays an important role. **b** The first two modes for our films with an external field of $B = 50 \text{ mT}$. A $k \parallel M_0$ cut-plane (thick blue, $n = 0$, and green, $n = 1$, lines) through their bowl like surfaces (light shading denotes surface in k_{\parallel}, k_{\perp}) is shown along with the 4-magnon resonant scattering pathway whereby two pumped magnons (orange dots on orange iso-frequency line for a pump frequency of 6.7 GHz) are converted into one $n = 0$ and one $n = 1$ magnon (blue and green points), the red dashed lines indicate scattering solutions that satisfy conservation of momenta and energy. The $n = 0$ band has minima at $k_{\parallel} \approx \pm 12 \text{ rads}/\mu\text{m}$, the $n = 1$ band has similar but less pronounced minima at $k_{\parallel} \approx \pm 4 \text{ rads}/\mu\text{m}$ (more details in section 1 of the SI) **c** Calculated normalized imaginary part of the 4-magnon scattering amplitude $\Psi_{1,2;3,4}$ (for detail see methods and SI). The inset shows the Feynman diagram corresponding to the one-loop correction. The different lines correspond to δ -function broadening of 0.5, 5 and 50 MHz. The peak in scattering occurs at the resonant pump frequency condition $\Omega \approx \omega_{\min n=0} + \omega_{\min n=1}$. **d** A phase diagram for magnon multi-band populations as a function of pumping power and frequency relative to the magnon modes (we show ΔF_p , the pump frequency relative to the bisection of the $k = 0$ frequency for $n = 0$ and $n = 1$ bands). The points are threshold data extracted from a field sweep and pump power sweep for a pump frequency of 7.15 GHz (see section 5 of the SI for more detail). The orange region shows the parametric pumping threshold. The blue region corresponds to occupation of the $n = 0$ minima, green region corresponds to occupation of the $n = 1$ minima, with the hatched region showing the multi-band occupation.

The material used for our experiments is yttrium iron garnet (YIG), a synthetic garnet with the lowest known magnon damping of any material. Due to this exceptional quality, it has been the subject of much research, from that focused on radar engineering in the 1960's^{20,21}, to the current work on magnonic devices^{22–29} and hybrid quantum systems^{30,31}. Perhaps most notably, in 2006 it was discovered by Demokritov et al.¹¹ to host a room temperature BEC of magnons, virtually unique as a room temperature realization of mesoscopic quantum phenomena in condensed matter. In YIG, magnon-magnon interactions leading to the thermalisation of the magnon gas act on nanosecond timescales, whereas magnon-phonon interactions lead to magnon losses over microseconds. The separation of these processes provides an opportunity to induce a quasi-equilibrium in the magnon system, and, under the right conditions, a unique room temperature magnon BEC. While the extent to which the room temperature magnon BEC in YIG should be understood as a genuine, stable BEC has been debated^{32,33}, there are a growing number of studies that show evidence for BEC-related properties such as spatial coherence³⁴, supercurrents³⁵ and sound modes in the condensate order parameter^{36,37} and very recent work has investigated the relative roles of

four-magnon and phonon-magnon interactions in leading to condensate formation and stability³⁸.

To move to a two-dimensional system analogous to the heterostructures studied for paired fermions we exploit advances in thin-film growth to produce the model confined magnon host constituted by thin (128 nm) YIG films grown on $\text{Gd}_3\text{Ga}_5\text{O}_{12}$ (GGG) substrates³⁹. In our work, we do not confine the magnons further, but others have studied the effectively one-dimensional systems constituted by narrow strips formed from such films, which display dramatically different mode structures as well as complex dynamics and enhanced lifetimes^{40,41} not seen for thicker and wider samples.

We used Brillouin light scattering (BLS) to directly measure the magnon populations in the films, subjected to static external magnetic field and excited by microwave fields delivered through a micropatterned transmission line; see Methods for details. Figure 2 shows spectra as a function of microwave pump power with a fixed frequency of 6.7 GHz, the resonance condition described by figure 1 for our films with a static field $B = 50 \text{ mT}$. The microwave drive is a burst excitation of length 500 ns and period $2.5 \mu\text{s}$. Without microwave excitation (figure 2 **a**), we observe thermal occupation of the magnons, with features corresponding to the $n = 0$ and $n = 1$ modes; the much broader spectrum for the $n = 0$ mode, with a cut-off at its minimum, and a sharper maximum for $n = 1$, are consistent with the dispersion surfaces of figure 1 **b**, which yield the theoretical density of states given by the solid line through the data (see SI for details). As the pump power is increased, we see a population corresponding to magnon pair formation, each at half the pump frequency (3.35 GHz), visible as the middle band/peak in figure 2 **b**. Following a further increase in pump power, magnon populations appear as sharp peaks (note the logarithmic vertical scale) in figure 2 **c** at the $n = 0$ and $n = 1$ minima. The observation of this pair of peaks constitutes the discovery of a multicomponent magnon condensate. The average signal corresponding to the different magnon populations plotted against pump power reveals two thresholds at $\sim 22 \text{ dBm}$ ($\sim 150 \text{ mW}$) for the parametric two-magnon pumping and $\sim 29 \text{ dBm}$ (800 mW) for the spontaneous formations at the $n = 0$ and $n = 1$ minima. A close inspection reveals that the $n = 0$ population first appears at powers just prior to the $n = 1$ population. Both populations follow a sharp threshold onset (see figure 2 **d**, note the log-log scale).

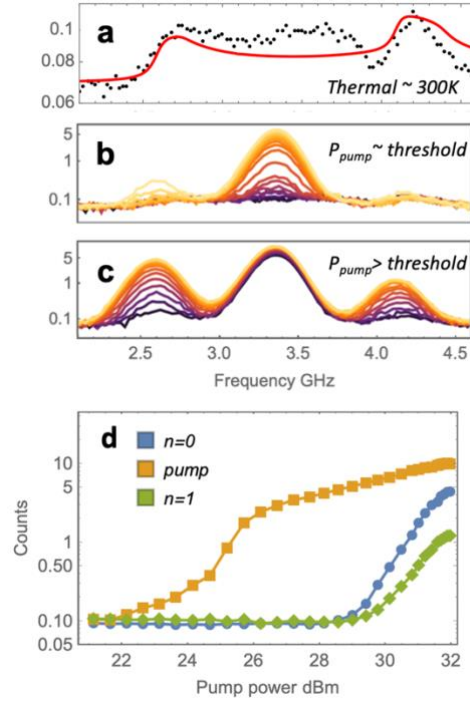


Figure 2: Magnon occupation for different pumping regimes.

a Thermal spectrum of magnons in the thin YIG film, the band from 2.5-3.75 GHz corresponds to the $n = 0$ mode, the peak at 4.1 GHz is related to the $n = 1$ mode, the red line is the fitted spectral function (see SI for details). **b** As the power is increased for a fixed frequency of 6.7 GHz, a population of magnon pairs due to parametric pumping appears at half the pump frequency ~ 3.5 GHz, and then the first signs of a population forming at the $n = 0$ minima ~ 2.6 GHz follow. **c** As the pump power is increased further magnon populations appear at both the $n = 0$ and $n = 1$ minima. **d** Signals for the different magnon populations as a function of pump power on a log-log scale, the onset of the condensation occurs ~ 6 dBm after the pumping threshold for visible magnon pairs.

The temporal evolution of the magnon spectrum and distinct magnon populations for different pump frequencies provide further insight into the Bose-Einstein condensation of the magnons (see figure 3). For the lowest pump frequency (6.45 GHz, first column in figure 3), we only see magnons at half the pump frequency and no spontaneous populations forming elsewhere. As we increase the pump frequency, there is the first sign of a spontaneous accumulation of magnons appearing at the $n = 0$ minima for 6.55 GHz. As the pump frequency is increased to satisfy the 4-magnon resonant condition where the total energy of two pumped magnons is approximately equal to mean of the $n = 0$ band and $n = 1$ bands, we see three distinct populations, the pumped magnons and those at the $n = 0$ and $n = 1$ minima, which have drastically enhanced lifetimes. For pump frequencies above this condition, we see a decrease in the magnon occupation at both the $n = 0$ and $n = 1$ minima accompanied by a growth in the signal at the intermediate frequencies.

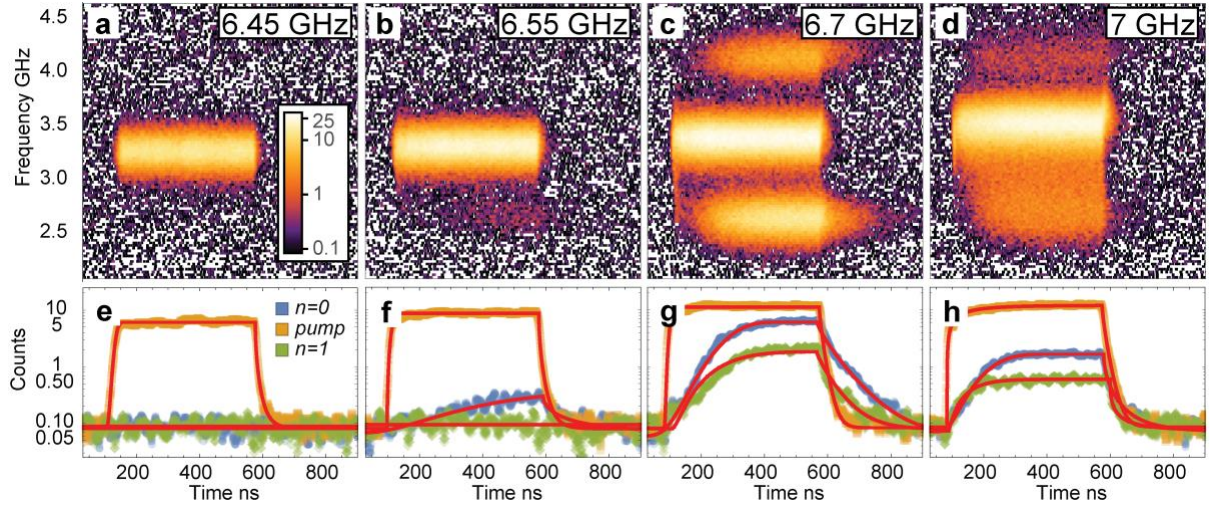


Figure 3: Time evolution of magnon populations in quantized thickness modes

a – d Temporal evolution of the full magnon spectrum for different pump frequencies. **e – h** Temporal evolutions at magnon frequencies corresponding to the $n = 0$ (blue) and $n = 1$ (green) minima and pumped (orange) populations. The red lines are fits of a piecewise function given in section 7 of the SI. There are three striking features in the data. First, the jump in the magnon populations at the $n = 0$ and $n = 1$ minima for the resonant 6.7 GHz pump. Second, the significantly enhanced lifetimes of the magnons at the $n = 0$ and $n = 1$ minima for this pumping condition. Finally, the transformation from three distinct magnon populations at 6.7 GHz to a broader distribution for higher pump frequencies.

Figure 4 **a** and **b** summarize the data as a function of excitation and measurement frequencies, and reveal how the magnon spectra change qualitatively from being dominated by a single peak due to parametrically pumped magnon pairs, then by two peaks, where the second corresponds to the $n = 0$ condensate, subsequently – at resonance - by three when the $n = 1$ condensate is also visible, and finally - above resonance – again by the single peak due to parametric pumping. In the latter case, the magnons in the $n = 0$ band yield a continuum underneath the peak at one-half of the pump frequency with weak maxima. This suggests that the “best” two-band condensate is obtained at resonance.

We can check the conjecture of an optimized condensate at resonance by looking in more detail at the time traces. In particular, a cursory examination of the traces in figure 3 **e-f** reveals that at resonance these decays are not only the slowest, but also that they seem non-exponential. To more precisely characterize the temporal evolution of the condensates, we fit stretched exponentials to the decay of different magnon populations:

$$f(t) = a \left(e^{-\left(\frac{t-t_0}{\tau}\right)^{n_d}} \right) + c \quad (1)$$

Model (1) quantifies the time scale of the population decay through the onset time t_0 , the exponential lifetime τ and the stretching exponent n_d . a and c are the amplitude and background respectively and are extracted directly from the data. The stretching exponent parametrizes a range of behaviours including those typically found for single-particle excitations coupled to a bath ($n_d = 1$) to the growth and decay of collective order in interacting many-body systems, including especially two-dimensional systems such as Ising magnets ($n_d = 0.5$) and polariton condensates ($n_d \approx 0.7$)^{42,43}. To assure that our conclusions concerning the decays are meaningful notwithstanding the number of available parameters and statistical errors, we attempt fits to the data assuming stretching exponents n_d fixed at 1.0 and 0.7 and evaluate the need for a non-trivial value $n_d \neq 1$ based on the Akaike information criterion (AIC)⁴⁴. The value of 0.7 was chosen for this analysis based on detailed examination of deviations of the data from eq. (1), as described in section 7 of the SI.

Tracking the fits of Eq. 1 as a function of pump frequency (see figure 4), we see a few clear trends in the behaviour of the different populations while pumping is below, on and above resonance. There are asymmetric peaks (figure 4 e) in the amplitudes of the populations at the $n = 0$ and $n = 1$ minima, with no signal below the resonance, a maximum at the resonance and a plateau above it. For the lifetimes (figure 4 f), the populations at the band minima also both show asymmetric enhancements, with a peak at the resonance pump frequency of 20-30 ns. Away from the resonance, the $n = 1$ lifetime falls to values similar to those of the pumped magnons (~10 ns), while the $n = 0$ population lifetime also falls off but not quite to the same extent. The nature of the $n = 0$ and $n = 1$ decay is shown to be qualitatively different from the pumped populations, the latter being agnostic with respect to the stretching exponent n_d and the former showing a strong preference (as measured by AIC difference) for the non-trivial value of 0.7 associated with an ordered system. Similarly as for the lifetime and amplitude this is enhanced asymmetrically around the resonance, with the $n = 1$ band behaving similarly to the pumped population above resonance whereas the $n = 0$ population continues to show a less pronounced preference for the nontrivial decay. The AIC comparison show that the condensate decays near resonance require a non-trivial n_d , i.e. the resonance condition produces decays of the type associated with other (quasi)ordered 2D systems such as polariton BEC's and Ising systems.

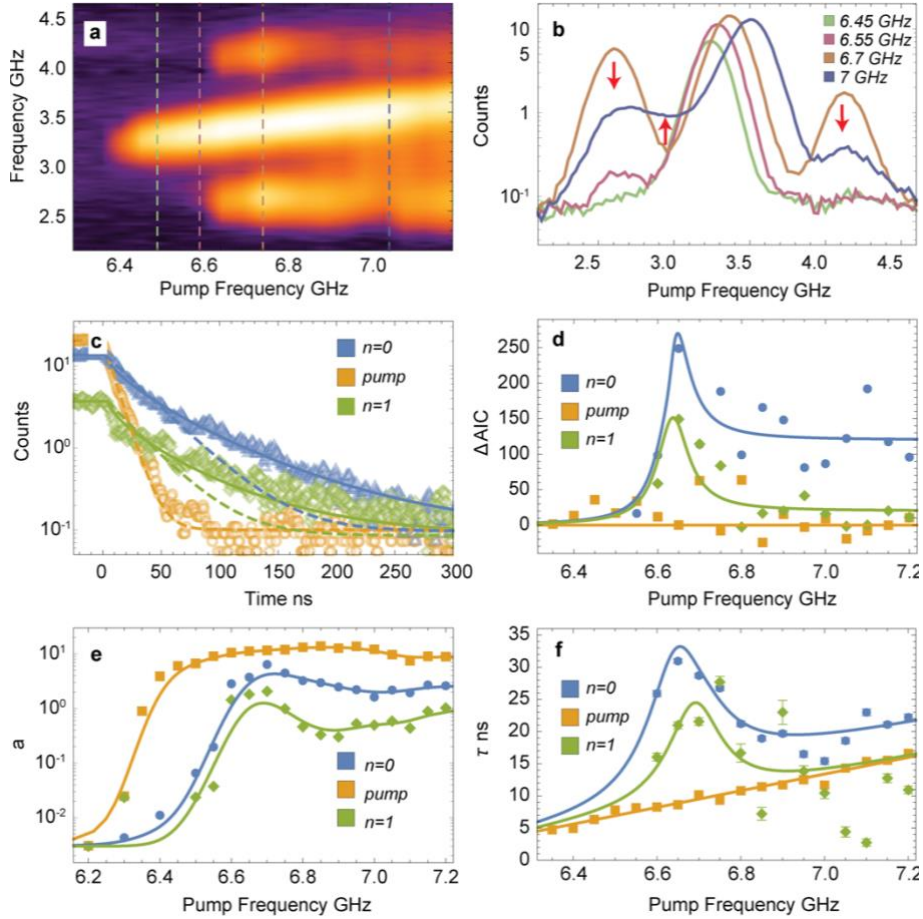


Figure 4: Dependence on pump frequency

a The magnon spectra as a function of pump frequency integrated over the time while the pump is applied. Colour scale is log of the magnon density. **b** Magnon spectra at fixed pump frequencies (slices denoted by corresponding dashed lines in **a**): 6.45 GHz where only the pumped population is excited, below resonance where the $n = 0$ condensate is first observed (6.55 GHz), at resonance, where the multiband condensate (6.7 GHz) is formed and above resonance (7.05 GHz). For the latter the magnons tend to decay through conventional non-resonant scattering down to the $n = 0$ mode, as visible by the growth in magnon signal at the intermediate frequencies highlighted by the red arrows. **c** Decay of the different populations at resonance (time relative to removal of the pump). While the pumped population can be fitted with a standard exponential (dashed lines – yellow), the $n = 0$ and $n = 1$ populations require a stretched exponential (solid lines – blue and green). **d** The difference in the Akaike information criterion (AIC) for models where n_d is fixed at 1 and 0.7 show the decay of the populations in the $n = 0$ and $n = 0$ bands, most notably on resonance, are best described by a stretched exponential decay commonly associated with (quasi)ordered 2D systems. **e-f** Amplitudes and decay times of the different magnon populations. We observe a clear peak in both amplitude and decay lifetime of the $n = 0$ and $n = 1$ populations at the resonant pumping conditions. Solid lines are guides to the eye and error bars are statistical errors from the fits.

The combination of threshold behaviour in relation to the pump power, the strongly enhanced lifetime following sub-exponential decay and the narrow distribution of magnon

energies at the frequencies corresponding to the minima for the $n = 0$ and $n = 1$ modes lead us to conclude that 1) the excited magnons are collected in populations near the dispersion minima, 2) nonlinear scattering processes enhance this mechanism at the resonant pump frequency rapidly redistributing magnons to the minima, tipping the magnon density over a critical threshold and resulting in a longer-lived multi-band condensate.

The resonant scattering that feeds the multi-band condensate is contrary to the thermalisation typically observed in single-band systems. Figure 4 **b** shows the integrated magnon spectra for different pump frequencies. At resonance, the signal in the magnon frequency range between the pumped population and the populations at the minima is very small, indicating that the resonant scattering injects magnons very close to the minima (further details given in section 6 of the SI). For conventional thermalisation one would expect a continuum, at least on the low-energy side of the pumped population, as magnons scatter down to the minimum via an incoherent magnon gas⁴⁵. Such behaviour is indeed recovered for higher pump frequencies (> 6.7 GHz), as seen by the *drop* in the density of magnons at the dispersion minima and *growth* for the intermediate magnon frequency (highlighted by arrows in figure 4 **b**). Another distinction between the scattering channels can be seen in the onset of the decay. In single band systems it is commonly observed that after the pump is switched off there is a delay and then a jump in the population at the minima prior to the decay starting. This is due to the conventional thermalisation scattering pathway in which the magnons must travel further through momenta space to reach the minimum. For the resonant case the redistribution is rapid and close to the minima, hence this delay is not observed whereas, again for higher non-resonant pumping the regular behaviour is recovered (figure 4 **c** and more details in section 7 of the SI). The differing energy and time scales of the magnon redistribution confirm that we have two scattering mechanisms at work, one is the conventional thermalisation of pumped magnons where magnons trickle down to the lowest energy available via an incoherent gas, and the other is the resonant mechanism anticipated theoretically as per figure 1, where magnons are scattered into the $n = 0$ and $n = 1$ bands.

Having established the detailed non-equilibrium dynamics of a multicomponent magnon BEC as a function of pump amplitude for fixed pump frequency, and as a function of pump frequency for fixed amplitude, it is natural to ask for a more general “phase diagram”, where the quotation marks imply that we are focusing only on signal intensities, as a function of both frequency and amplitude, in analogy with the phase diagrams associated with complex order parameters in fermionic systems where the tuning parameters are typically temperature, pressure and magnetic field. It turns out that it is more convenient to vary the

external magnetic field on the sample as a proxy for the frequency. Surveying our system using the external field to tune the magnon mode frequency and varying RF pump power (pump frequency fixed at 7.15 GHz) reveals a complex phase diagram (see figure 1 **d**). For high fields (>85 mT) the magnon bands are above the pump half-frequency and no magnons can be excited. As the field is lowered, the half-frequency of the pump aligns directly with the $n = 0$ magnon band minima and a single component population is established at relatively low power, likewise, for the $n = 1$ band minima at the much lower field (~30 mT). For most intermediate fields, magnons are injected into the $n = 0$ band away from its minima, however, they still populate it due to thermalisation via magnon-magnon interactions. Finally, for a specific intermediate field (~60 mT) the relation of both bands and the pump frequency is such that there is excitation of magnons into both bands simultaneously (the hatched region in figure 1 **d**). This occurs at the resonance condition prescribed by the Feynman diagram of Figure 1 **a**, i.e. when the pump frequency approximately bisects the $n = 0$ and $n = 1$ band minima $\omega_p \approx \omega_{min\ n=0} + \omega_{min\ n=1}$.

We have discovered that thin films of high-quality YIG host a room temperature non-equilibrium multi-band magnon BEC in both the $n = 0$ and $n = 1$ $k \parallel M_0$ magnon branches. The formation of the BEC is driven primarily by a resonant scattering process, and indeed evidence for long-lived collective dynamics in this two-dimensional system is only obvious at resonance. The observed behaviour is counter to the much-studied single-band situation where pumped magnons thermalise by passing through a gaseous incoherent phase before reaching the band minima³⁵. As we move off resonance, the quantity and quality (measured e.g., by post-pumping lifetime and deviation from trivial exponential decay) of condensate diminish because magnons are scattered away from the band minima. These magnons engage more effectively in scattering events which reduce the condensate population.

Thus, the physics in figure 1, namely a multiparticle scattering resonance leading to an optimized multicomponent BEC in a two-band system, appears validated. Furthermore, what we see bears phenomenological resemblance to the celebrated Feshbach resonance⁴⁶ which underpins the science of cold atoms, as well as the optimized pairing instability found at the Lifschitz transition where a second quantum well state is occupied for the two-dimensional electronic system constituted by (100) LaAlO₃/SrTiO₃. Given the widespread interest but limited experimental platforms and available theory, our experiments obviously suggest more detailed studies including some to determine whether the resemblances are somehow meaningful. More importantly they open a new and straightforward route to create and understand multicomponent condensates and their collective behaviour, including novel

normal modes and topological excitations. Particularly exciting opportunities are associated with the ease of imaging magnons in YIG using new techniques such as diamond NV sensors⁴⁷ and soft X-ray microscopy^{23,24}. The resonance underpinning the multi-component BEC reported could also be exploited in semiclassical and quantum devices where efficient generation and switching of magnons with sharply peaked momentum distributions is required.

Methods

Modelling of magnon dynamics

A more detailed discussion of the spin-wave spectrum, spectral function and scattering process are given in SI sections 1, 2 and 3 respectively.

The simultaneous appearance of the peaks in the magnon populations at $n = 0$ and $n = 1$ branches is linked to the enhancement of the scattering amplitude and, consequently, four-magnon scattering terms in the collision integral. The corresponding Feynman diagram and the normalised imaginary part of the first-order correction to the scattering amplitude are shown in figure 1 **c**. The explicit expression for the imaginary part of the scattering amplitude reads as

$$Im \Psi_{1,2;3,4}(\Omega, \mathbf{K}) = -\pi \sum_{n,n'=0,1} \int \frac{d^2k}{(2\pi)^2} |\Psi_{1,2;3,4}^0|^2 \{n_B[\Omega - \omega_n(\mathbf{K} - \mathbf{k})] - n_B[\omega_{n'}(\mathbf{k})]\} \delta[\Omega - \omega_n(\mathbf{K} - \mathbf{k}) - \omega_{n'}(\mathbf{k})], \quad (2)$$

where n and n' denote the lowest and the second-lowest magnon branches respectively and n_B is the Bose-Einstein distribution. We focus on the process where two pumped magnons (denoted by subscripts 1 and 2) are created due to the splitting of the same photon, $\mathbf{K} = \mathbf{0}$. For simplicity, we ignore the momentum dependence of the zero-order scattering amplitude $\Psi_{1,2;3,4}^0$. The peak in $Im \Psi_{1,2;3,4}(\Omega, \mathbf{0})$ appears because the additional scattering channel to the $n = 1$ magnon branch opens up at $\omega_p \geq \omega_{min\ n=0} + \omega_{min\ n=1}$. The details of the calculations are provided in section 4 of the SI.

Samples

The single-crystalline YIG films were grown on (111) GGG substrates by liquid-phase epitaxy (LPE) on 1-inch GGG wafer from a PbO-B₂O₃-based high-temperature solution using a standard dipping technique^{39,48}. The 128 nm-thin YIG LPE film showed excellent spin wave damping with a full width at half maximum FMR linewidth of 1.0 Oe at 6.5 GHz and a Gilbert damping parameter $\alpha = 5 \times 10^{-5}$, giving FMR lifetimes of ~ 350 ns. For RF excitation $2 \mu\text{m}$

wide 200 nm thick Cu striplines were patterned on the samples by electron beam lithography and lift-off processing. To mitigate the otherwise significant charging during exposure an Aluminium layer was deposited on top of the resist. A micrograph of the completed devices is shown in SI section 10.

Time-resolved Brillouin Light Scattering microspectroscopy

We used a micro-BLS set-up with temporal (~ 0.8 ns) and spatial resolution (~ 300 nm) to measure the magnon dynamics in our sample. The frequency of the incident light is shifted by inelastic scattering from magnons in the sample, thus the measurement of light intensity for a given frequency shift can be correlated with the density of magnons of said frequency. The experimental set-up consists of a 473 nm CW laser with an incident power of 0.85 mW focused through an objective lens with $NA = 0.85$. The laser is focussed on the frontside (YIG film facing) to the side of the strip-line. The reflected light is sent through a specialised Fabry-Perot interferometer^{33,39} and detected with a single photon counting detector. Quoted values for counts with non-integer values due to averaging per unit time. The RF excitation is supplied by a signal generator (Anritsu) with high-speed switches, rise time ~ 2 ns (Universal Microwave Components Corporation), controlling the pulse characteristics. For the phase diagram, a burst of 150 ns with a period 300 ns and pump frequency of 7.15 GHz was used. For the detailed time-resolved measurements, a burst of 500 ns with a period 2500 ns was used with a varying pump frequency and power. This latter measurement was explicitly configured to extract the temporal dynamics of the populations i.e., giving us a maximum temporal resolution of 0.8 ns and 'off period' for the RF ~ 50 x the observed decay times. All the quoted powers are instantaneous power onto the sample. The spectrometer, photon detector and switches are all locked to a common clock such that photon detection events are then binned both in frequency shift and time. The sample is magnetized in plane using a permanent magnet and orientated such that the micropatterned transmission line is perpendicular to the external field, in the so-called parallel pumping configuration.

Data analysis

For the measurements of magnon dynamics for varying pump power and pump frequency, the different magnon populations were distinguished by separate frequency windows. These windows were determined via a fit of the sum of 3 normal distributions (for BLS, the Gaussian smoothing due to the poor frequency resolution of the instrument dominates all other line shapes) with a constant background. The centre of each of these 3 normal distributions was taken to be the central frequency of each population. The frequency window around the central frequency was defined as the mean full width at half maximum

determined by the fits and common for all populations. In particular for the 50mT sweeps shown in figures 2-4, the frequency windows for the 0th order populations, pumped magnons and 1st order populations, with pump frequency 6.7 GHz were found to be: 2.59, 3.35 and 4.12 +/- 0.13GHz. There was found to be a small frequency offset (0.15 GHz) between the pumped magnon populations and the set pump frequency, which was due to the calibration of the spectrometer. Therefore, all reported frequencies are shifted to take this into account.

References

1. Bose. Plancks Gesetz und Lichtquantenhypothese. *Zeitschrift für Phys.* **26**, 178–181 (1924).
2. Einstein, A. Quantentheorie des einatomigen idealen Gases. *Sitzungsber. Kgl. Preuss. Akad. Wiss* **261**, (1924).
3. Einstein, A. Quantentheorie des einatomigen idealen Gases. *Sitzungsber. Kgl. Preuss. Akad. Wiss.* **3**, (1925).
4. Bardeen, J., Cooper, L. N. & Schrieffer, J. R. Theory of superconductivity. *Phys. Rev.* **108**, 1175–1204 (1957).
5. Leggett, A. J. Number-Phase Fluctuations in Two-Band Superconductors. *Prog. Theor. Phys.* **36**, 901–930 (1966).
6. Leggett, A. J. Bose-Einstein condensation in the alkali gases: Some fundamental concepts. *Rev. Mod. Phys.* **73**, 307–356 (2001).
7. Iskin, M. & Sá De Melo, C. A. R. Two-band superfluidity from the BCS to the BEC limit. *Phys. Rev. B - Condens. Matter Mater. Phys.* **74**, 144517 (2006).
8. Zhang, Y. C., Ding, S. & Zhang, S. Collective modes in a two-band superfluid of ultracold alkaline-earth-metal atoms close to an orbital Feshbach resonance. *Phys. Rev. A* **95**, 041603 (2017).
9. Rinott, S. *et al.* Tuning across the BCS-BEC crossover in the multiband superconductor Fe_{1+y}SexTe_{1-x}: An angle-resolved photoemission study. *Sci. Adv.* **3**, e1602372 (2017).
10. Blumberg, G. *et al.* Observation of Leggett's collective mode in a multiband MgB₂ superconductor. *Phys. Rev. Lett.* **99**, 227002 (2007).
11. Demokritov, S. O. *et al.* Bose-Einstein condensation of quasi-equilibrium magnons at room temperature under pumping. *Nature* **443**, 430–433 (2006).
12. Höfer, M. *et al.* Observation of an Orbital Interaction-Induced Feshbach Resonance in Yb 173. *Phys. Rev. Lett.* **115**, 265302 (2015).
13. Binnig, G., Baratoff, A., Hoenig, H. E. & Bednorz, J. G. Two-band superconductivity in

- Nb-Doped SrTiO₃. *Phys. Rev. Lett.* **45**, 1352–1355 (1980).
14. Mukuda, H. *et al.* Multiband superconductivity in heavy fermion compound CePt 3Si without inversion symmetry: An NMR study on a high-quality single crystal. *J. Phys. Soc. Japan* **78**, (2009).
 15. Ponomarev, Y. G. *et al.* Evidence for a two-band behavior of MgB₂ from point-contact and tunneling spectroscopy. *Solid State Commun.* **129**, 85–89 (2004).
 16. Mourik, V. *et al.* Signatures of Majorana fermions in hybrid superconductor-semiconductor nanowire devices. *Science (80-.)*. **336**, 1003–1007 (2012).
 17. Albrecht, S. M. *et al.* Exponential protection of zero modes in Majorana islands. *Nature* **531**, 206–209 (2016).
 18. Singh, G. *et al.* Gap suppression at a Lifshitz transition in a multi-condensate superconductor. *Nat. Mater.* **18**, 948–954 (2019).
 19. Mikkelsen, A. E. G., Kotetes, P., Krogstrup, P. & Flensberg, K. Hybridization at Superconductor-Semiconductor Interfaces. *Phys. Rev. X* **8**, 031040 (2018).
 20. De Wames, R. E. & Wolfram, T. Characteristics of magnetostatic surface waves for a metalized ferrite slab. *J. Appl. Phys.* **41**, 5243–5246 (1970).
 21. Eshbach, J. R. & Damon, R. W. Surface magnetostatic modes and surface spin waves. *Phys. Rev.* **118**, 1208–1210 (1960).
 22. Qin, H., Both, G. J., Hämäläinen, S. J., Yao, L. & van Dijken, S. Low-loss YIG-based magnonic crystals with large tunable bandgaps. *Nat. Commun.* **9**, (2018).
 23. Förster, J. *et al.* Direct observation of coherent magnons with suboptical wavelengths in a single-crystalline ferrimagnetic insulator. *Phys. Rev. B* **100**, 214416 (2019).
 24. Förster, J. *et al.* Nanoscale X-ray imaging of spin dynamics in yttrium iron garnet. *J. Appl. Phys.* **126**, (2019).
 25. Chumak, A. V., Serga, A. A. & Hillebrands, B. Magnon transistor for all-magnon data processing. *Nat. Commun.* **5**, (2014).
 26. Wang, Q. *et al.* A magnonic directional coupler for integrated magnonic half-adders. *Nat. Electron.* **3**, 765–774 (2020).
 27. Talmelli, G. *et al.* Reconfigurable submicrometer spin-wave majority gate with electrical transducers. *Sci. Adv.* **6**, 4042–4060 (2020).
 28. Barman, A. *et al.* The 2021 Magnonics Roadmap. *J. Phys. Condens. Matter* (2021) doi:10.1088/1361-648x/abec1a.
 29. Dieny, B. *et al.* Opportunities and challenges for spintronics in the microelectronics industry. *Nature Electronics* vol. 3 446–459 (2020).
 30. Tabuchi, Y. *et al.* Coherent coupling between a ferromagnetic magnon and a superconducting qubit. *Science (80-.)*. **349**, 405–408 (2015).
 31. Zhang, D. *et al.* Cavity quantum electrodynamics with ferromagnetic magnons in a

- small yttrium-iron-garnet sphere. *npj Quantum Inf.* **1**, 1 (2015).
32. Rückriegel, A. & Kopietz, P. Rayleigh-Jeans Condensation of Pumped Magnons in Thin-Film Ferromagnets. *Phys. Rev. Lett.* **115**, 157203 (2015).
 33. Tupitsyn, I. S., Stamp, P. C. E. & Burin, A. L. Stability of Bose-Einstein condensates of hot magnons in Yttrium iron garnet films. *Phys. Rev. Lett.* **100**, 1–4 (2008).
 34. Nowik-Boltyk, P., Dzyapko, O., Demidov, V. E., Berloff, N. G. & Demokritov, S. O. Spatially non-uniform ground state and quantized vortices in a two-component Bose-Einstein condensate of magnons. *Sci. Rep.* **2**, 1–5 (2012).
 35. Bozhko, D. A. *et al.* Supercurrent in a room-temperature Bose-Einstein magnon condensate. *Nat. Phys.* **12**, 1057–1062 (2016).
 36. Tiberkevich, V. *et al.* Excitation of coherent second sound waves in a dense magnon gas. *Sci. Rep.* **9**, (2019).
 37. Bozhko, D. A. *et al.* Bogoliubov waves and distant transport of magnon condensate at room temperature. *Nat. Commun.* **10**, (2019).
 38. Schneider, M. *et al.* Bose–Einstein condensation of quasiparticles by rapid cooling. *Nat. Nanotechnol.* **15**, 457–461 (2020).
 39. Dubs, C. *et al.* Sub-micrometer yttrium iron garnet LPE films with low ferromagnetic resonance losses. *J. Phys. D: Appl. Phys.* **50**, 204005 (2017).
 40. Mohseni, M. *et al.* Bose-Einstein condensation of nonequilibrium magnons in confined systems. *New J. Phys.* **22**, 083080 (2020).
 41. Mohseni, M. *et al.* Controlling the Nonlinear Relaxation of Quantized Propagating Magnons in Nanodevices. *Phys. Rev. Lett.* **126**, 097202 (2021).
 42. Huse, D. A. & Fisher, D. S. Dynamics of droplet fluctuations in pure and random Ising systems. *Phys. Rev. B* **35**, 6841–6846 (1987).
 43. Caputo, D. *et al.* Topological order and thermal equilibrium in polariton condensates. *Nat. Mater.* **17**, (2018).
 44. Akaike, H. A New Look at the Statistical Model Identification. *IEEE Trans. Automat. Contr.* **19**, 716–723 (1974).
 45. Dzyapko, O., Demidov, V. E., Melkov, G. A. & Demokritov, S. O. Bose-Einstein condensation of spin wave quanta at room temperature. *Trans. R. Soc. A* **369**, 3575–3587 (2011).
 46. Feshbach, H. Unified theory of nuclear reactions. *Ann. Phys. (N. Y.)* **5**, 357–390 (1958).
 47. Du, C. *et al.* Control and local measurement of the spin chemical potential in a magnetic insulator. *Science (80-.)*. **357**, 195–198 (2017).
 48. Dubs, C. *et al.* Low damping and microstructural perfection of sub-40nm-thin yttrium iron garnet films grown by liquid phase epitaxy. *Phys. Rev. Mater.* **4**, 024416 (2020).

Data Availability

The data that support the findings of this study are available from the corresponding author upon request.

Acknowledgements

J.B. was supported from the European Union's Horizon 2020 Research and Innovation Programme under the Marie Skłodowska-Curie Grant Agreement No. 66566. Work of G.A., A.B., J.B. and P.S. was supported by the European Research Council under the European Union's Seventh Framework Program Synergy HERO SYG-18 810451. AB and PS were also supported by the University of Connecticut, Yale University, the Knut and Alice Wallenberg Foundation KAW 2018.0104 and Villum Fonden. K.B. is supported by the SNSF via 16301. C.D. acknowledges the financial support from the Deutsche Forschungsgemeinschaft (DFG, German Research Foundation) - 271741898. Giancarlo Corradini (EPFL) is thanked for his assistance with wire bonding the samples and Oleksii Surzhenko (INNOVENT) for the FMR line width measurements

Author Contributions:

JB and GA designed and conceived the experiments. CD produced the thin films of YIG. SF and SW produced the samples with the support of JR. JB and KB performed the BLS measurements with the support of DG and GA. JB performed the data analysis. JB, PS and AB developed the magnon population models. PS and AB developed the magnon scattering theory. JB and GA wrote the manuscript with the help of PS and AB. All authors aided in discussions and interpretation of results.

Ethics declarations

The authors declare no competing interests.

Additional Information

Supplementary Information is available for this paper

Correspondence and requests for materials should be addressed to Joe Bailey (joe.bailey@psi.ch) or Gabriel Aeppli (gabriel.aeppli@psi.ch)